Investigation into the effect of Si doping on the performance of $Sr_{1-y}Ca_yMnO_{3-\delta}$ SOFC cathode materials†

Jose M. Porras-Vazquez,*[a] Enrique R. Losilla,[b] Philip J. Keenan,[a] Cathryn A. Hancock,[a] Thomas F. Kemp,[c] John V. Hanna*[c] and Peter R. Slater*[a]

In this paper we report the successful incorporation of silicon into $Sr_{1-y}Ca_yMnO_{3-\delta}$ perovskite materials for potential applications in cathodes for solid oxide fuel cells. The Si substitution onto the B site of a ^{29}Si enriched $Sr_{1-y}Ca_yMn_{1-x}Si_xO_{3-\delta}$ perovskite system is confirmed by ^{29}Si MAS NMR measurements at low B_0 field. The very large paramagnetic shift (~3000–3500 ppm) and anisotropy (span ~4000 ppm) suggests that the Si^{4+} species experiences both Fermi contact and electron-nuclear dipolar contributions to the paramagnetic interaction with the $Mn^{3+/4+}$ centres. An improvement in the conductivity is observed for low level Si doping, which can be attributed to two factors. The first of these is attributed to the tetrahedral coordination preference of Si leading to the introduction of oxide ion vacancies, and hence a partial reduction of Mn^{4+} to give mixed valence Mn. Secondly, for samples with high Sr levels, the undoped systems adopt a hexagonal perovskite structure containing face sharing of MnO_6 octahedra, while Si doping is shown to help to stabilise the more highly conducting cubic perovskite containing corner linked octahedra. The level of Si, x, required to stabilise the cubic $Sr_{1-y}Ca_yMn_{1-x}Si_xO_{3-\delta}$ perovskite in these cases is shown to decrease with increasing Ca content; thus cubic symmetry is achieved at $x = 0.05$ for the $Sr_{0.5}Ca_{0.5}Mn_{1-x}Si_xO_{3-\delta}$ series; $x = 0.075$ for $Sr_{0.7}Ca_{0.3}Mn_{1-x}Si_xO_{3-\delta}$; $x = 0.10$ for $Sr_{0.8}Ca_{0.2}Mn_{1-x}Si_xO_{3-\delta}$; and $x = 0.15$ for $SrMn_{1-x}Si_xO_{3-\delta}$. Composites with 50% $Ce_{0.9}Gd_{0.1}O_{1.95}$ were examined on dense $Ce_{0.9}Gd_{0.1}O_{1.95}$ pellets. For all series an improvement in the area specific resistances (ASR) values is observed for the Si-doped samples. Thus these preliminary results show that silicon can be incorporated into perovskite cathode materials and can have a beneficial effect on the performance.

1. Introduction

Perovskite manganites have attracted considerable interest due to potential applications as cathode materials in the field of solid oxide fuel cells (SOFCs). Traditionally doping strategies for such materials have focused on substitution with cations of similar size, *e.g.* Sr for La.[1–5] In this study we investigate an alternative strategy, the incorporation of silicate. The approach employed stems from prior observations on the successful incorporation of oxyanions into perovskite-type cuprate superconductors and related phases.[6–14] This work demonstrated that the perovskite structure can incorporate significant levels of oxyanions (carbonate, borate, nitrate, sulfate, phosphate). In such samples, the C, B, N, P, S of the oxyanion group was shown to reside on the perovskite B cation site, with the oxide ions of this group filling 3 (C, B, N)–4 (P, S) of the available 6 oxide ion positions around this site. Recently we have illustrated the potential of this oxyanion doping strategy in perovskite-type materials with potential for use in solid oxide fuel cells.[15–17] For instance, phosphate and sulphate were successfully incorporated in $SrCoO_3$-type materials, leading to an enhancement of the electronic conductivity, attributed to a change from a 2H- to a 3C-perovskite.[15] More recently, phosphate and borate were also introduced in $Ba_{1-x}Sr_xCo_{0.8}Fe_{0.2}O_3$-type materials with a small improvement in the electronic conductivity for low levels of doping, along with improved thermal stability, as demonstrated by long term annealing studies at intermediate temperatures.[16] Similarly, borate and phosphate

[a]*School of Chemistry, University of Birmingham, Birmingham, B15 2TT, UK. E-mail: j.m.porras@bham.ac.uk, p.r.slater@bham.ac.uk; Fax: +44 (0)1214144403; Tel: +44 (0)1214148672*

[b]*Depto de Química Inorgánica, Cristalografía y Mineralogía, Universidad de Málaga, Málaga, 29071, Spain*

[c]*Department of Physics, University of Warwick, Coventry, CV4 7AL, UK. E-mail: j.v.hanna@warwick.ac.uk*

†Electronic supplementary information (ESI) available. See DOI: 10.1039/c3dt32561j

were also successfully incorporated in $CaMnO_3$ and La_{1-x}-Sr_xMnO_3 with improvements in the electronic conductivity and in the ASR values with respect to the parent compounds.[17] This doping strategy has also been successfully applied to potential electrolyte systems, with such work showing that phosphate, silicate and sulphate could be introduced into the ionic conductors $Ba_2(In/Sc)_2O_5$ leading to a structural change from brownmillerite, containing ordered oxide ion vacancies, to a highly conducting cubic perovskite, where the oxide ion vacancies are disordered.[18–21] ^{29}Si and ^{31}P-NMR of such systems confirmed the tetrahedral coordination of Si/P within the structure So far our studies on electrode systems have mainly focused on phosphate and borate. In this work, we extend such studies to a detailed investigation of the effect of the incorporation of silicate groups. This is of particular interest, since silica is widely considered a detrimental contaminant of SOFC materials, particularly electrolyte materials, as it has been reported to segregate at the grain boundaries where it forms insulating siliceous phases, lowering the conductivity, such that overall performance is degraded.[22–28] For example, it has been reported that several hundreds ppm of SiO_2 can increase the electrolyte grain boundary resistance by over one order of magnitude.[29–31]

Our preliminary studies on Si incorporation were performed in cobalt-based perovskite electrode materials, showing the successful incorporation of Si into $La_{0.6}Sr_{0.4}Co_{0.8}Fe_{0.2}O_{3-\delta}$ and $Sr_{1-x}Y_xCoO_{3-\delta}$-based materials, with significant results in term of improvements in the conductivity and an enhancement in the stability towards CO_2.[32] Similarly, Si doping was shown to be successful in the manganese/cobalt-based perovskite electrode materials, $SrMO_{3-\delta}$ (M=Co, Mn).[33] The silicon doping was shown to be successful results in terms of stabilization of the 3C-perovskite containing corner linked octahedra (the undoped composition is a 2H perovskite, containing face sharing of octahedra), and a consequent enhancement in the conductivity. However, for $SrMnO_{3-\delta}$, quite high levels (15%) of Si were required to stabilise the 3C-perovskite, and while the Si doping is beneficial in this respect, it might also be expected to show some detrimental effect in terms of partially disrupting the electronic conducting pathways. Therefore, in this work we have examined mixed calcium–strontium, Sr_yCa_{1-y}-$MnO_{3-\delta}$ systems, with a view to lowering the Si level needed to achieve this stabilisation. In this paper we therefore report studies into the effect of Si doping into $Sr_yCa_{1-y}MnO_3$ and its effect on the electrical properties to examine the potential for SOFC applications. As a comparison to Si doping, another isovalent dopant, Ti, was also examined for selected systems.

The characterisation of these Si doped systems has been undertaken using XRD, TGA, SEM, impedance measurements and ^{29}Si solid state MAS NMR spectroscopy. The ^{29}Si MAS NMR measurements reported within provide the first unambiguous demonstration of the Si incorporation occurring directly into the perovskite structure of such manganite systems.

2. Experimental

$SrCO_3$ (Aldrich, 99.9%), $CaCO_3$ (Aldrich, 99%), MnO_2 (Aldrich, 99%), SiO_2 (Aldrich, 99.6%), TiO_2 (Aldrich, 99.8%) were used to prepare $Sr_yCa_{1-y}Mn_{1-x}A_xO_{3-\delta}$ ($y = 0$, 0.5, 0.7, 0.8 and 1; $x \leq$ 0.175; A = Si and Ti). For the $CaMn_{1-x}Si_xO_{3-\delta}$ series, the powders were intimately ground and heated initially to 1200 °C for 12 h. They were then ball-milled (350 rpm for 1 hour, Fritsch Pulverisette 7 Planetary Mill) and reheated to 1250 °C for a further 12 h. For the $Sr_yCa_{1-y}Mn_{1-x}Si_xO_{3-\delta}$ series ($y = 0.5$, 0.7, 0.8 and 1), the powders were intimately ground and heated initially to 1300 °C for 12 h. They were then ball-milled (350 rpm for 1 hour) and reheated to 1350 °C for a further 12 h. For the ^{29}Si solid state MAS NMR spectroscopic studies ^{29}Si enriched samples were formulated following the same synthetic procedure but using ^{29}Si-enriched SiO_2 (Cortecnet, 97.1%) as the ^{29}Si source. For the physical mixture, $Sr_{0.8}Ca_{0.2}MnO_3$ and the appropriate amount of ^{29}Si-enriched SiO_2 were mixed and ground together in order to represent a theoretical doping level of Si = 0.1 and provide a standard to monitor the possibility of the formation of phase separated of SiO_2.

Powder X-ray diffraction (XRD) (Bruker D8 diffractometer with Cu Kα_1 radiation) was used to demonstrate phase purity, as well as for cell parameters determination. For the latter, the GSAS suite of programs was used.[34]

Oxygen contents were estimated from thermogravimetric analysis (Netzsch STA 449 F1 Jupiter Thermal Analyser), a method commonly used in the determination of the oxygen content in cathode materials.[35–37] Samples were heated at 10 °C min^{-1} to 1200 °C in N_2 and held for 30 minutes to reduce the Mn oxidation state to 3+. This is consistent with prior reports on the reduction of undoped $SrMnO_3$ to $Sr_2Mn_2O_5$.[38] The original oxygen content and average Mn oxidation state then was determined from the mass loss observed.

Pellets for conductivity measurements were prepared as follows: the powders were first ball-milled (350 rpm for 1 hour), before pressing (200 MPa) as pellets and sintering at 1350 °C for 12 h. Conductivities were then measured using the four probe dc method. Four Pt electrodes were attached with Pt paste, and then the sample was fired to 800 °C in air for 1 hour to ensure bonding to the sample. The samples were then furnace cooled to 350 °C in air and held at this temperature for 12 hours to ensure full oxygenation.

The morphology of the sintered pellets was studied using a JEOL SM-6490LV scanning electron microscope. The ceramic surfaces were polished with diamond spray from 6 to 1 mm of diameter and then thermally etched at 50 °C below the sintering temperature for 15 min at a heating/cooling rate of 5 °C min^{-1}. Finally, the samples were sputtered with graphite for better image definition.

To elucidate the potential of these materials as SOFC cathodes, symmetrical electrodes were coated on both sides of dense $Ce_{0.9}Gd_{0.1}O_{1.95}$ (CGO10, Aldrich) pellets (sintered at 1500 °C for 12 h) using a suspension prepared with a mixture

of electrolyte and electrodes (1 : 1 wt%) and Decoflux™ (WB41, Zschimmer and Schwarz) as binder material. The symmetrical cells were fired at 900 °C for 1 h in air. Afterwards, a Pt-based ink was applied onto the electrodes to obtain a current collector layer and finally fired at 800 °C for 1 hour. Area-specific resistance (ASR) values were then obtained under symmetrical air atmosphere in a two electrode configuration. Impedance spectra of the electrochemical cells were collected using a HP4912A frequency analyser, at open circuit voltage (OCV), in the 5 Hz–13 MHz frequency range with ac signal amplitude of 100 mV. The spectra were fitted to equivalent circuits using the ZView software,[39] which allows an estimation of the resistance and capacitance associated with the different cell contributions.

All ^{29}Si MAS NMR measurements were performed on a low field Chemagnetics CMX-100 spectrometer (B_0 = 2.35 T) operating at a [29]Si Lamor frequency of 29.88 MHz. MAS NMR experiments were undertaken using a Doty 4 mm MAS probe in which MAS frequencies (ν_r) of 15 kHz were achieved. Pulse time calibration was performed on a sample of solid kaolinite where a B_1 field of 83 kHz delivered a $\pi/2$ pulse width of 4 μs. The ^{29}Si MAS NMR data were acquired using both single pulse and rotor-synchronised spin echo ($\theta - \tau - 2\theta - \tau$) experiments. Single pulse measurements used a $\pi/4$ flip angle which equated to an excitation pulse width of 2 μs, while the rotor-synchronised spin echo experiments utilised $\theta/2\theta$ flip angles of $\pi/4$/ $\pi/2$ (2/4 μs, respectively) and a τ delay of 50 μs. The reported [29]Si chemical shifts are referenced to the primary IUPAC standard of TMS (δ 0 ppm) via a secondary solid standard of kaolinite (δ −92 ppm) which was also used for the pulse time calibration. Single pulse measurements which focussed on diamagnetic components within each sample used recycle delays of 60 s, while the spin echo experiments were used to study the paramagnetic component of these samples which permitted much shorter recycle delays of 0.25 s to be implemented.

3.   Results and discussion

Solid solution range

First of all, it is necessary to state the symmetry of the undoped samples, i.e. $Sr_yCa_{1-y}MnO_{3-\delta}$. The calcium endmember ($y = 0$) composition, $CaMnO_{3-\delta}$, is orthorhombic, while for strontium ($y = 1$), $SrMnO_{3-\delta}$, it is hexagonal. For the mixed Ca/ Sr samples, $Sr_yCa_{1-y}MnO_{3-\delta}$, there is gradual transition from the orthorhombic to the hexagonal form as the strontium content increases.

For the Ca endmember samples, $CaMn_{1-x}Si_xO_{3-\delta}$, X-ray diffraction data showed the successful incorporation of silicon up to $x = 0.05$ with no change in cell symmetry on doping. Higher dopant amounts led to the segregation of secondary phases, such as $Ca_4Mn_3O_{10}$ (PDF 089-5427). For these doped compositions, although they were still orthorhombic, the difference between the a and c parameters became lower, suggesting that the silicon doping increases the "tetragonality" of this series (see Table 1). If we examine the ratio a/c for this series we can see that this number decreases from 1.0030 for $CaMnO_{3-\delta}$ to values around 1.0008 for the doped compositions. Confirmation of the introduction of silicate was shown by the fact that equivalent Mn deficient samples $CaMn_{1-x}O_{3-\delta}$ ($x = 0.05$) with no added silicate gave the segregation of secondary phases, such as $Ca_4Mn_3O_{10}$.

For the $Sr_yCa_{1-y}Mn_{1-x}Si_xO_{3-\delta}$ series ($y = 0.5$, 0.7 and 0.8), single phase samples could be achieved up to higher levels of silicon, $x \leq 0.125$. As for Si doping in $CaMnO_{3-\delta}$, exceeding this Si content led to the segregation of secondary phases. Without Si doping, the samples were shown to be either hexagonal perovskites (at high Sr levels, $y = 0.8$) as for the Sr endmember, $SrMnO_{3-\delta}$, a mixture of hexagonal and cubic perovskites ($y = 0.7$), or a mixture of tetragonal and orthorhombic ($y = 0.5$). As the silicon content was increased, the level of cubic perovskite was increased, with the amount of silicon needed to produce a single phase cubic perovskite sample increasing as the strontium content increases (Fig. 1). The single phase cubic samples were achieved at $x = 0.05$ for the $Sr_{0.5}Ca_{0.5}Mn_{1-x}Si_xO_{3-\delta}$ series, $x = 0.075$ for $Sr_{0.7}Ca_{0.3}Mn_{1-x}Si_xO_{3-\delta}$, and $x = 0.10$ for $Sr_{0.8}Ca_{0.2}Mn_{1-x}Si_xO_{3-\delta}$, which compares to $x = 0.15$ for $SrMn_{1-x}Si_xO_{3-\delta}$ in our previous study.[33] The Rietveld refinement for $Sr_{0.7}Ca_{0.3}Mn_{0.925}Si_{0.075}O_3$ is shown in Fig. S1.† The figure shows a very good fit with very low R factors (R_{wp} = 2.40% and R_F = 1.43%). In addition the Bragg reflections for this composition are marked and it can be seen that there are no secondary phases. Moreover, if we refine the occupancy factors for the Ca and Sr and the Mn and Si pairs, the values are very close to the theoretical values. Similar results and R factors are obtained for the rest of the samples.

In Fig. 2, SEM micrographs are shown for (a) $Sr_{0.5}Ca_{0.5}MnO_{3-\delta}$; (b) $Sr_{0.5}Ca_{0.5}Mn_{0.95}Si_{0.05}O_{3-\delta}$; (c)

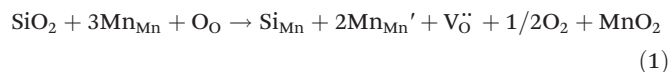**Table 1** Cell parameters and normalised cell volumes for $Sr_yCa_{1-y}Mn_{1-x}Si_xO_{3-\delta}$ ($y = 0$ and 0.5; $x \leq 0.15$)

$Sr_yCa_{1-y}Mn_{1-x}Si_xO_{3-\delta}$

Sr (y)	0			0.5		
Si (x)	0	0.05	0.10	0	0.10	0.15
a (Å)	5.2673(1)	5.2800(2)	5.2929(5)	5.3308(11)	3.7916(1)	3.7988(2)
b (Å)	5.2828(1)	5.2855(3)	5.2967(4)	5.3303(12)	3.7916(1)	3.7988(2)
c (Å)	7.4575(1)	7.4682(3)	7.4770(6)	7.5448(3)	3.7916(1)	3.7988(2)
V/Z (Å^3)	51.89(1)	52.10(1)	52.40(4)	53.60(2)	54.51(1)	54.82(1)

$Sr_{0.7}Ca_{0.3}MnO_{3-\delta}$ and (d) $Sr_{0.7}Ca_{0.3}Mn_{0.925}Si_{0.075}O_{3-\delta}$. Comparing $Sr_{0.5}Ca_{0.5}MnO_{3-\delta}$ and $Sr_{0.5}Ca_{0.5}Mn_{0.95}Si_{0.05}O_{3-\delta}$, there is no significant difference in the morphology on Si doping. In the case of $Sr_{0.7}Ca_{0.3}MnO_{3-\delta}$, the SEM micrographs show evidence for striations on the grains, consistent with strain effects. These strain effects can be explained by the fact that hexagonal

Fig. 1 X-ray diffraction patterns for (a) $Sr_{0.7}Ca_{0.3}MnO_{3-\delta}$; (b) $Sr_{0.7}Ca_{0.3}Mn_{0.925}Si_{0.075}O_{3-\delta}$; (c) $Sr_{0.7}Ca_{0.3}Mn_{0.9}Si_{0.1}O_{3-\delta}$; (d) $Sr_{0.8}Ca_{0.2}MnO_{3-\delta}$; (e) $Sr_{0.8}Ca_{0.2}Mn_{0.925}Si_{0.075}O_{3-\delta}$; and (f) $Sr_{0.8}Ca_{0.2}Mn_{0.9}Si_{0.1}O_{3-\delta}$. Hexagonal perovskite peaks marked with asterisks.

Fig. 2 SEM micrographs for (a) $Sr_{0.5}Ca_{0.3}MnO_{3-\delta}$; (b) $Sr_{0.5}Ca_{0.5}Mn_{0.95}Si_{0.05}O_{3-\delta}$; (c) $Sr_{0.7}Ca_{0.3}MnO_{3-\delta}$ and (d) $Sr_{0.7}Ca_{0.3}Mn_{0.925}Si_{0.075}O_{3-\delta}$.

perovskites typically transform to cubic perovskites at elevated temperatures (e.g. those used in the sintering), reverting slowly back to hexagonal perovskites on cooling. In contrast, the grains for the Si doped sample, $Sr_{0.7}Ca_{0.3}Mn_{0.925}Si_{0.075}O_{3-\delta}$, showed no such evidence of strain effects, which can be explained by both the low temperature and high temperature structure being cubic, and thus there being no phase changes on heating and cooling.

Cell parameters for these systems were determined from the X-ray diffraction data using the Rietveld method (see Tables 1 and 2). The change in cell parameters for these oxyanion doped perovskite materials is a balance between the effect of the smaller size of Si^{4+}, which would be expected to lead to a reduction in cell volume, and the associated reduction in the average Mn oxidation state, which would be expected to lead to an increase in cell volume. In line with prior works on manganite systems, mixed valence $Mn^{3+/4+}$ is assumed, although there is a possibility that Si incorporation may locally stabilize some Mn^{2+}. The partial reduction of Mn^{4+} through Si doping is predicted by the following defect equation, assuming tetrahedral coordination for Si and reduction to Mn^{3+}, which illustrates that for each Mn replaced by Si a reduction of $2Mn^{4+}$ to Mn^{3+} would be predicted.

$$SiO_2 + 3Mn_{Mn} + O_O \rightarrow Si_{Mn} + 2Mn_{Mn}' + V_O^{\cdot\cdot} + 1/2O_2 + MnO_2 \quad (1)$$

As can be seen from the above equation, a key driving force for the reduction of Mn is the introduction of oxide ion vacancies due to the lower coordination (tetrahedral rather than octahedral) preference of the Si dopant (i.e. for $x = 0$, the B cation site is completely occupied by 6 coordinate Mn, while for $x > 0$ some Si is on this site, with the tetrahedral coordination preference leading to a reduction in the total oxygen content). Thus, while we are nominally performing an isovalent (Si^{4+} in place of Mn^{4+}) substitution, the generation of oxide ion vacancies results in partial reduction, i.e. electron doping. The stabilization of the cubic perovskite polymorph on silicon doping can then be related to the lower average Mn oxidation state, and hence average B cation size, reducing the tolerance factor. The difference in Si content required to achieve this stabilisation across the $Sr_yCa_{1-y}MnO_{3-\delta}$ series can be explained by the fact that for samples with the highest levels of Sr, the average size of the A site is higher, and hence the starting tolerance factor for the parent phase is higher.
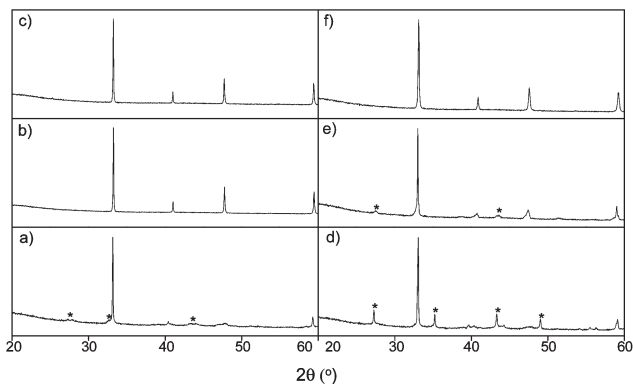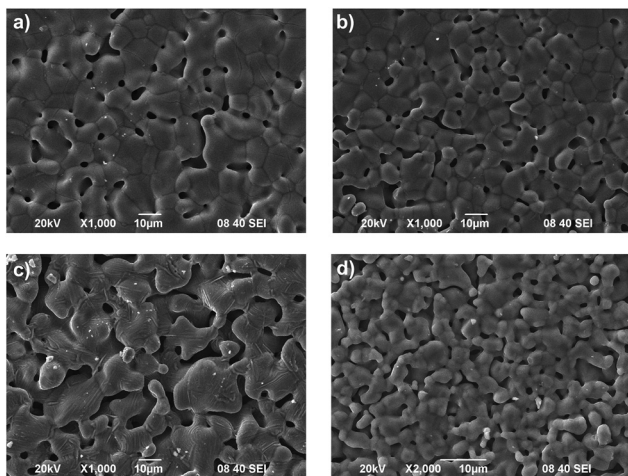
Table 2 Cell parameters and normalised cell volumes for $Sr_yCa_{1-y}Mn_{1-x}Si_xO_{3-\delta}$ ($y = 0.7$, 0.8 and 1; $x \le 0.175$)

$Sr_yCa_{1-y}Mn_{1-x}Si_xO_{3-\delta}$									
Sr (y)	0.7			0.8			1		
Si (x)	0	0.075	0.1	0	0.10	0.125	0	0.15	0.175
a (Å)	5.3963(1)	3.7988(1)	3.8019(1)	5.4072(1)	3.8127(2)	3.8157(2)	5.4481(1)	3.8380(3)	3.8456(3)
b (Å)	9.3424(1)	3.7988(1)	3.8019(1)	9.3755(1)	3.8127(2)	3.8157(2)	5.4481(1)	3.8380(3)	3.8456(3)
c (Å)	9.1208(1)	3.7988(1)	3.8019(1)	9.0990(1)	3.8127(2)	3.8157(2)	9.0796(2)	3.8380(3)	3.8456(3)
V/Z (Å^3)	57.47(2)	54.82(2)	54.95(1)	57.66(2)	55.42(1)	55.55(1)	58.35(1)	56.53(1)	56.87(3)

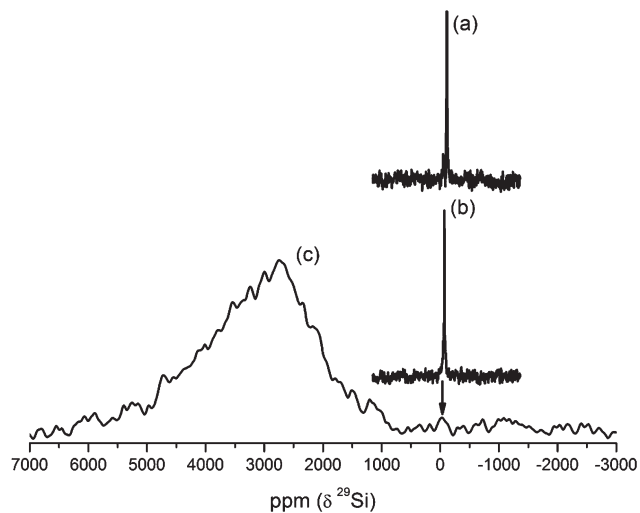**Fig. 3** Low field (B_0 = 2.35 T) solid state ^{29}Si MAS NMR data for (a) the physical mixture of ^{29}SiO$_2$ and Sr$_{0.8}$Ca$_{0.2}$MnO$_3$ (δ −113 ppm), and (b, c) the ^{29}Si doped Sr$_{0.8}$Ca$_{0.2}$Mn$_{0.9}$Si$_{0.1}$O$_{3−\delta}$ (δ −70 ppm and ∼3000–3500 ppm). The data from the ^{29}SiO$_2$/Sr$_{0.8}$Ca$_{0.2}$MnO$_3$ physical mixture in (a) and the narrow component from the doped Sr$_{0.8}$Ca$_{0.2}$Mn$_{0.9}$^{29}Si$_{0.1}$O$_{3−\delta}$ system in (b) were acquired at ambient temperature with a single pulse experiment and an MAS frequency of ν_r = 15 kHz. The broad data from the doped Sr$_{0.8}$Ca$_{0.2}$Mn$_{0.9}$^{29}Si$_{0.1}$O$_{3−\delta}$ system in (c) was acquired with a rotor synchronised spin echo experiment with ν_r = 15 kHz and a frequency offset of +35 kHz.
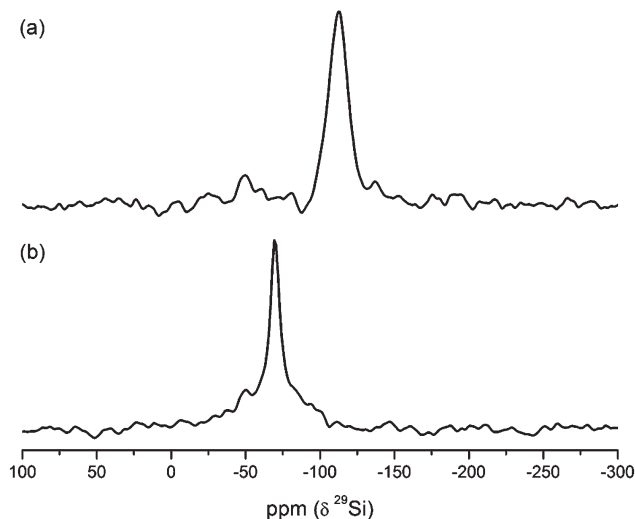

Fig. 4 Expansion of the solid state ^{29}Si MAS NMR data for (a) the physical mixture of ^{29}SiO$_2$ and Sr$_{0.8}$Ca$_{0.2}$MnO$_3$ (δ −113 ppm), and (b) ^{29}Si doped Sr$_{0.8}$Ca$_{0.2}$Mn$_{0.9}$Si$_{0.1}$O$_{3−\delta}$ (δ −70 ppm), acquired at low B_0 field (2.35 T) and at ambient temperature. These data were acquired using a single pulse experiment and ν_r = 15 kHz.

Consequently, it is necessary to reduce a larger amount of Mn^{4+} to Mn^{3+} and hence introduce a larger Si content.

Direct evidence for Si^{4+} incorporation into the perovskite structure is provided by the low field ^{29}Si MAS NMR results shown in Fig. 3. This figure compares the data obtained from a physical (highly ground) mixture of ^{29}Si enriched SiO$_2$ with undoped Sr$_{0.8}$Ca$_{0.2}$MnO$_{3−\delta}$ (see Fig. 3a), and that acquired from a ^{29}Si doped Sr$_{0.8}$Ca$_{0.2}$Mn$_{0.9}$Si$_{0.1}$O$_{3−\delta}$ sample (see Fig. 3b and c). As observed from Fig. 3a and the expansion of this data shown in Fig. 4a, the ^{29}SiO$_2$/Sr$_{0.8}$Ca$_{0.2}$MnO$_{3−\delta}$ mixture yields a single ^{29}Si resonance with a chemical shift δ −113 ppm which is characteristic of the ^{29}SiO$_2$ component only. However, similar measurements on the ^{29}Si doped Sr$_{0.8}$Ca$_{0.2}$Mn$_{0.9}$Si$_{0.1}$O$_{3−\delta}$ system produces two very different signals; one narrow resonance that occurs downfield from the ^{29}SiO$_2$ resonance at δ −70 ppm (see Fig. 3b and 4b), and one very broad resonance with a large downfield shift of ∼3000–3500 ppm (see Fig. 3c). From the narrow linewidth and long T_1 (>180 s) characterising the δ −70 ppm resonance it is concluded that it represents a diamagnetic impurity phase formed under the Si incorporation conditions, and the chemical shift suggests that it's likely to be a strontium/calcium silicate phase. In this respect, this sample did indeed show very weak impurities, such as Sr$_2$SiO$_4$. It has been previously reported that the chemical shift for Si is −69.42 ppm,[40] very close to the experimental value determined, −70 ppm. The significantly broadened resonance centred at ∼3000–3500 ppm shown in Fig. 3c was acquired with a rotor synchronised spin echo experiment using a short recycle delay of 0.25 s. These characteristics establish that this

is a paramagnetically influenced Si species in the Sr$_{0.8}$Ca$_{0.2}$Mn$_{0.9}$Si$_{0.1}$O$_{3−\delta}$ structure which is probably experiencing both Fermi contact and electron-nuclear dipolar contributions within the overall paramagnetic interaction with the Mn centres, as evidenced by the large paramagnetic shift and broad anisotropic lineshape spanning ∼4000 ppm, respectively. These data, therefore, provide the first direct evidence of Si incorporation into the perovskite framework in such manganite perovskites. The tetrahedral environment of silicon is not possible to state due to the fact that its resonance is paramagnetically influenced and very displaced. The only previous reports of Si in perovskites relates to their high interest for earth scientists, where perovskites such as CaSiO$_3$, and MgSiO$_3$ are believed to be the main components of the earth's lower mantle. These studies have shown that to achieve octahedral Si, extremely high pressures are required, and at lower pressures Si will be tetrahedral. It is therefore quite reasonable to propose tetrahedral coordination for Si and indeed this tetrahedral coordination helps to explain the observed reduction in the Mn oxidation state and enhancement in conductivity/change to a cubic cell.

The average oxidation states of Mn in these systems are reported in Table 3, and as can be seen, the average oxidation states are closer to 3 as the silicon content increases. Overall the oxygen contents determined from TGA, suggest that once the cubic perovskite forms, further loss of oxygen occurs, since the oxygen contents determined are lower than the value assuming eqn (1) is the only origin of oxide ion vacancies (*e.g.* for 5% Si doping, a stoichiometry of CaMn$_{0.95}$Si$_{0.05}$O$_{2.95}$ might be predicted from eqn (1), while TGA studies indicated a lower oxygen content, CaMn$_{0.95}$Si$_{0.05}$O$_{2.8}$).

An illustration of the importance of the lower coordination preference of Si (4 *versus* 6 for Mn) in these systems is shown

Table 3 Oxygen deficiencies (δ), Mn oxidation states (from TGA), conductivity data at 700 °C and ASR values at 800 °C for $Sr_yCa_{1-y}Mn_{1-x}Si_xO_{3-\delta}$ series. The error estimated for the oxygen deficiencies and manganese oxidation states from the noise of the TGA line are ±0.01 and ±0.02 respectively

$Sr_yCa_{1-y}Mn_{1-x}Si_xO_{3-\delta}$										
Sr (y)	0		0.5		0.7		0.8		1	
Si (x)	0	0.05	0	0.10	0	0.075	0	0.10	0	0.15
Oxygen deficiency (δ)	0.04	0.20	0.01	0.27	~0	0.29	~0	0.31	~0	0.23
Oxidation state	3.93	3.56	3.98	3.41	~4	3.37	~4	3.31	~4	3.23
Conductivity at 700 °C (S cm^{-1})	3.2	38.1	2.5	34.2	0.4	29.5	0.3	24.9	0.01	11.2
Conductivity at 800 °C (S cm^{-1})	7.6	40.2	3.4	36.3	0.7	30.4	0.6	26.1	0.03	14.0
ASR at 700 °C (Ω cm^2)	12.3	3.49	11.07	1.21	0.70	0.44	1.60	0.49	1.23	0.67
ASR at 800 °C (Ω cm^2)	1.50	0.35	1.73	0.20	0.11	0.08	0.36	0.07	0.20	0.09

by a comparison with Ti-doped $Sr_{1-x}Ca_xMnO_{3-\delta}$ samples: $SrMn_{0.85}Ti_{0.15}O_{3-\delta}$ and $Sr_{0.8}Ca_{0.2}Mn_{0.9}Ti_{0.1}O_{3-\delta}$. As in the case of Si-doping, for these latter Ti doped systems, we are also nominally performing an isovalent (Ti^{4+} in place of Mn^{4+}) substitution. However, in this case we do not expect any reduction of Mn^{4+} or generation of oxide vacancies, due to the preference of the Ti for octahedral coordination, as for the Mn, rather than the tetrahedral coordination of Si. Therefore, Ti-doping is not expected to lead to any decrease in the average Mn oxidation state, and, thus, no change in the symmetry from the undoped compositions to the Ti-doped ones for low level Ti doping. If we examine the XRD patterns of $SrMn_{0.85}Ti_{0.15}O_{3-\delta}$ and $Sr_{0.8}Ca_{0.2}Mn_{0.9}Ti_{0.1}O_{3-\delta}$, we can see that the predicted behaviour is confirmed, *i.e.* the cubic form is not stabilized (Fig. S2†). This illustrates that it is the oxygen vacancies incorporated as a result of the lower coordination of Si that are key to the beneficial effects on Si doping.

Conductivity measurements. For the Ca endmember systems, $CaMn_{1-x}Si_xO_{3-\delta}$, the undoped composition showed low conductivities (1.9–7.6 S cm^{-1} between 600–800 °C), as expected, due to the lack of significant mixed valence. For all doped samples a large improvement in the conductivity was observed, which can be attributed to the introduction of mixed valency as illustrated by defect eqn (1). The maximum conductivity values were reached for $x = 0.05$ (43.0–52.8 S cm^{-1} between 600–800 °C) (Fig. 5).

As for the $CaMn_{1-x}Si_xO_{3-\delta}$ systems, the mixed Sr/Ca systems, $Sr_yCa_{1-y}Mn_{1-x}Si_xO_{3-\delta}$ showed very low conductivities between 600 and 800 °C for the samples without Si ($x = 0$): 0.16–0.57 S cm^{-1}, for $Sr_{0.8}Ca_{0.2}MnO_{3-\delta}$; 0.17–0.70 S cm^{-1}, for $Sr_{0.7}Ca_{0.3}MnO_{3-\delta}$; and 1.7–3.4 S cm^{-1} for $Sr_{0.5}Ca_{0.5}MnO_{3-\delta}$. The low conductivities can be attributed to the lack of significant mixed valency, as well as the presence of poorly conducting hexagonal perovskite. In all doped compositions there is an improvement in conductivity, even for the Si-doped samples where complete conversion to the cubic perovskite has not occurred. The highest conductivity values were, however, reached for the samples which XRD showed were single phase cubic perovskites; *i.e.* $x = 0.10$ for $Sr_{0.8}Ca_{0.2}Mn_{1-x}Si_xO_{3-\delta}$ (23.1–26.1 S cm^{-1}, between 600–800 °C) and $x = 0.05$ for $Sr_{0.5}Ca_{0.5}Mn_{1-x}Si_xO_{3-\delta}$ (31.5–36.3 S cm^{-1}); and $x = 0.075$ for $Sr_{0.7}Ca_{0.3}Mn_{1-x}Si_xO_{3-\delta}$ (28.0–30.4 S cm^{-1}). Fig. 6 shows the

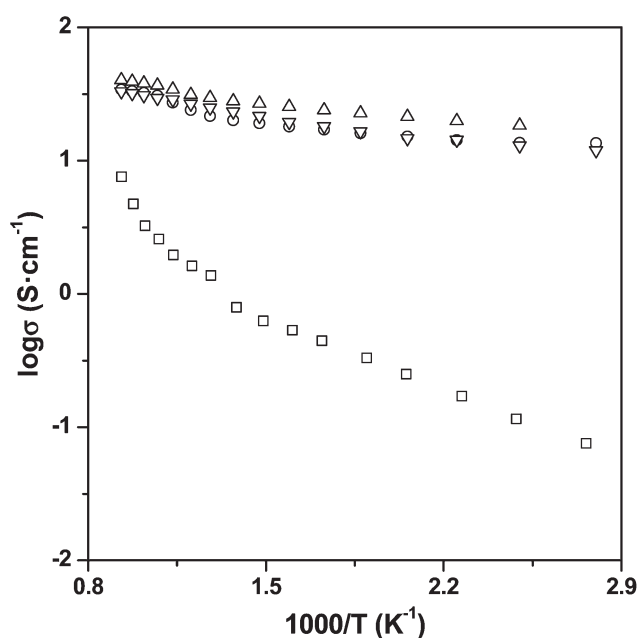**Fig. 5** Plot of log σ vs. $1000/T$ for $CaMnO_{3-\delta}$ ($\square$), $CaMn_{0.975}Si_{0.025}O_{3-\delta}$ ($\bigcirc$), $CaMn_{0.95}Si_{0.05}O_{3-\delta}$ ($\triangle$) and $CaMn_{0.90}Si_{0.10}O_{3-\delta}$ ($\triangledown$).

temperature dependence of the conductivity for $Sr_{0.8}Ca_{0.2}Mn_{1-x}Si_xO_{3-\delta}$ series. All other series show a similar behaviour.

As shown previously,[33] for the strontium endmember samples, $SrMn_{1-x}Si_xO_{3-\delta}$, the undoped ($x = 0$) composition showed very low conductivities, 0.008–0.03 S cm^{-1} between 600–800 °C, while the Si doped samples for which a cubic perovskite was observed ($x \geq 0.15$) showed much higher conductivities. The highest conductivity values were achieved for $x = 0.15$ (24.0–29.4 S cm^{-1} between 600–800 °C).

Overall the results from this work show a significant enhancement in the conductivity on Si doping, with the maximum conductivity for all series matching the composition with the minimum Si content that achieves the full stabilization of the cubic form. Increasing the Si contents beyond this amount led to lower conductivities, likely due to a partial disruption of the electronic conduction pathways by silicon at these high doping levels. This conclusion is consistent with the fact that maximum conductivity observed for these Si
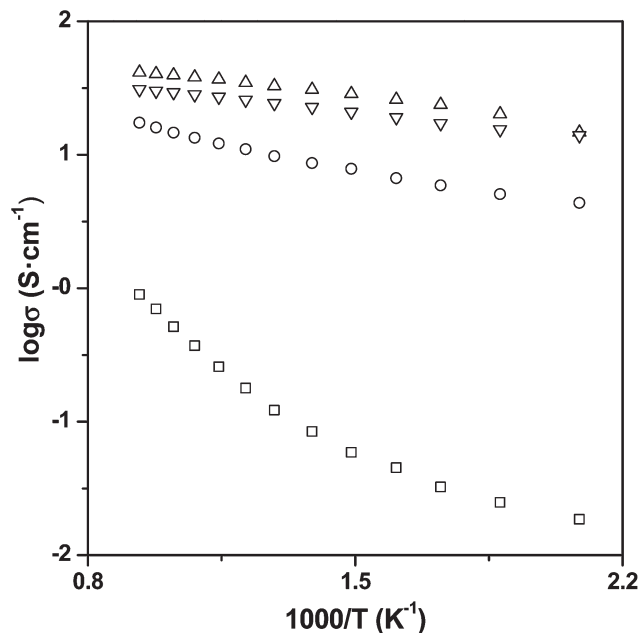
Fig. 6 Plot of log σ vs. 1000/T for $Sr_{0.8}Ca_{0.2}MnO_{3-\delta}$ ($\square$), $Sr_{0.8}Ca_{0.2}Mn_{0.925}Si_{0.075}O_{3-\delta}$ (O), $Sr_{0.8}Ca_{0.2}Mn_{0.9}Si_{0.1}O_{3-\delta}$ ($\triangle$) and $Sr_{0.8}Ca_{0.2}Mn_{0.875}Si_{0.125}O_{3-\delta}$ ($\triangledown$).

Fig. 7 Impedance spectra of the symmetrical cells for $SrMnO_3$ ($\square$) and $SrMn_{0.85}Si_{0.15}O_{3-\delta}$ ($\blacksquare$)/CGO10 composites at 700 °C. The serial resistance was subtracted for better comparison of the spectra.

Fig. 8 Plot of log(area-specific resistance (ASR)) vs. 1000/T for $SrMnO_{3-\delta}$ ($\blacksquare$), $SrMn_{0.85}Si_{0.15}O_{3-\delta}$ ($\square$), $Sr_{0.8}Ca_{0.2}MnO_{3-\delta}$ ($\bullet$), $Sr_{0.8}Ca_{0.2}Mn_{0.90}Si_{0.10}O_{3-\delta}$ (O), $CaMnO_{3-\delta}$ ($\blacktriangle$) and $CaMn_{0.95}Si_{0.05}O_{3-\delta}$ ($\triangle$).

doped samples decreases in moving across the series from $CaMnO_{3-\delta}$ to $SrMnO_{3-\delta}$, since for the latter end higher Si contents are necessary to stabilise the cubic perovskite and hence achieve this maximum.

Area-specific resistance study. Following the promising conductivity results, cathode testing was performed for both the samples without Si doping, as well as the Si doped samples which showed the highest conductivities. These experiments used a composite of the perovskite and CGO10 (1 : 1 wt%) on dense CGO10 pellets. For all series, the XRD patterns of the samples and CGO10 mixtures show no evidence of additional diffraction peaks due to impurities at temperatures up to 900 °C (Fig. S3†). At 1000 °C, however, there were weak extra peaks, indicating some reaction between the system and CGO. The reaction product has been identified as $Ca_4Mn_3O_{10}$ (PDF 089-0815) and $Sr_3Mn_2O_7$ (PDF 024-1217). Consequently the composite deposition temperature was limited to 900 °C.

In Fig. 7, we show the impedance spectra for the symmetrical cells with $SrMnO_3$/CGO10 and $SrMn_{0.85}Si_{0.15}O_{3-\delta}$/CGO10 cathodes. The spectra can be decomposed into two overlapped contributions, a high frequency arc (assigned to the transport of O^{2-} ions and intermediate species through the cathode and at the cathode–electrolyte interface), and a low frequency arc (assigned to the competitive reactions at the TPB: adsorption, transfer of species and surface diffusion).[41] As can be seen, the two phenomena are much smaller for the Si-doped sample, which can be explained by the increase in electronic conductivity and likely also oxide ion conductivity (due to the generation of oxide ion vacancies caused by the oxyanion doping).

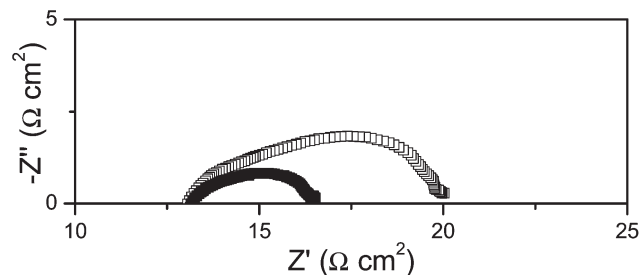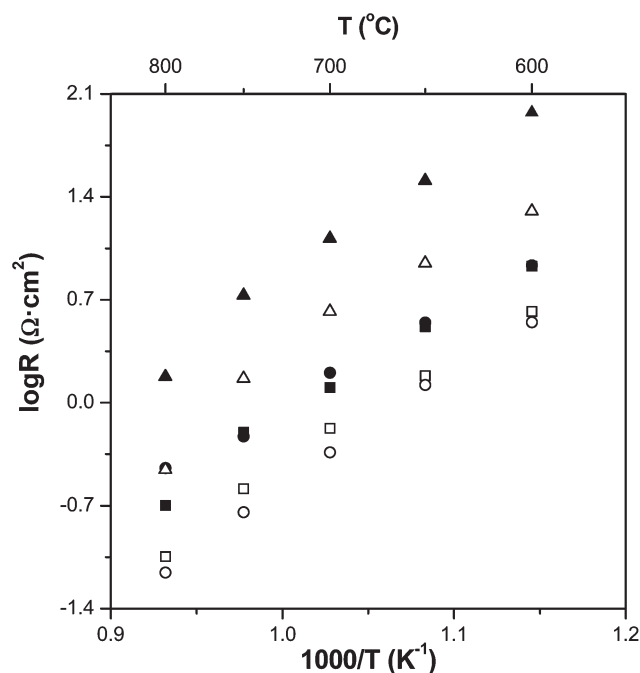The dependences of ASR with temperature are shown in Fig. 8 and Table 3. For all series an improvement in the ASR

values was observed for the Si-doped samples with respect to the undoped compositions. For instance, for $CaMn_{0.95}Si_{0.05}O_3$, $Sr_{0.7}Ca_{0.3}Mn_{0.925}Si_{0.075}O_3$ and $SrMn_{0.85}Si_{0.15}O_3$, the values obtained at 800 °C, were 0.35, 0.08 and 0.09 Ω cm^2 respectively, and these results entail a significant improvement with respect to the corresponding samples without Si doping: 1.50, 0.11 and 0.20 Ω cm^2 for $CaMnO_3$, $Sr_{0.7}Ca_{0.3}MnO_3$ and $SrMnO_3$, respectively. We can see that there is a non-linear behaviour of the ASR data, with a bigger drop in the values at the higher temperatures. This behaviour is likely due to the greater loss of oxygen at high temperature, causing a higher amount of oxide vacancies and a better oxide ion mobility and ASR values. Thus, in this work we show that in addition to enhancing the conductivities, silicon doping has a positive effect on the ASR of the perovskite-CGO cathode composites. Overall the lowest

ASR values were observed for the Sr rich systems, which may be related to improved oxide ion conduction in such systems as a result of the increase in cell size.

4. Conclusions

$Sr_yCa_{1-y}Mn_{1-x}Si_xO_{3-\delta}$ cathode materials have been prepared by solid state reaction, and direct evidence for the incorporation of Si into the structure provided for the first time by ^{29}Si NMR. In each case, Si doping is shown to enhance the conductivity, which can be attributed to electron doping (driven by the introduction of oxide ion vacancies due to the preference for Si to adopt tetrahedral coordination), as well as a change from a hexagonal (containing face sharing of octahedra) to a cubic perovskite (containing corner sharing of octahedra) for samples with high levels of Sr. For the latter, the level of Si needed to stabilise the cubic perovskite increases with increasing Sr content. Cathode (perovskite-CGO composites) testing showed an improvement in the ASR values for the Si-doped samples with respect to the undoped compositions. Thus, these preliminary results show that silicon doping can have a beneficial effect on the performance of perovskite manganite cathode materials, provided that it is accommodated within the perovskite structure.

Acknowledgements

References

1 A. Orera and P. R. Slater, *Chem. Mater.*, 2010, **22**, 675.
2 A. J. Jacobson, *Chem. Mater.*, 2010, **22**, 660.
3 A. Lastaberg and S. J. Skinner, *J. Mater. Chem.*, 2006, **16**, 3161.
4 J. H. Kuo, H. U. Anderson and D. M. Sparlin, *J. Solid State Chem.*, 1990, **87**, 55.
5 H. Yokokawa, N. Sakai, T. Kawada and M. Dokiya, *Solid State Ionics*, 1990, **40–41**, 398.
6 C. Greaves and P. R. Slater, *J. Mater. Chem.*, 1991, **1**, 17.
7 C. Greaves and P. R. Slater, *Physica C*, 1991, **175**, 172.
8 P. R. Slater, C. Greaves, M. Slaski and C. M. Muirhead, *Physica C*, 1993, **208**, 193.
9 Y. Miyazaki, H. Yamane, N. Ohnishi, T. Kajitani, K. Hiraga, Y. Mori, S. Funahashi and T. Hirai, *Physica C*, 1992, **198**, 7.
10 A. Maignan, M. Hervieu, C. Michel and B. Raveau, *Physica C*, 1993, **208**, 116.
11 K. Kinochita and T. Yamada, *Nature*, 1992, **357**, 313.
12 B. Raveau, M. Hervieu, D. Pelloquin, C. Michel and R. Retoux, *Z. Anorg. Allg. Chem.*, 2005, **631**, 1831.
13 D. Pelloquin, M. Hervieu, C. Michel, N. Nguyen and B. Raveau, *J. Solid State Chem.*, 1997, **134**, 395.
14 V. Caignaert, B. Domenges and B. Raveau, *J. Solid State Chem.*, 1995, **120**, 279.
15 C. A. Hancock, R. C. T. Slade, J. R. Varcoe and P. R. Slater, *J. Solid State Chem.*, 2011, **184**, 2972.
16 J. M. Porras-Vazquez and P. R. Slater, *J. Power Sources*, 2012, **209**, 180.
17 J. M. Porras-Vazquez, T. F. Kemp, J. V. Hanna and P. R. Slater, *J. Mater. Chem.*, 2012, **22**, 8287.
18 J. F. Shin, L. Hussey, A. Orera and P. R. Slater, *Chem. Commun.*, 2010, **46**, 4613.
19 J. F. Shin, D. C. Apperley and P. R. Slater, *Chem. Mater.*, 2010, **22**, 5945.
20 J. F. Shin and P. R. Slater, *J. Power Sources*, 2011, **196**, 8539.
21 J. F. Shin, K. Joubel, D. C. Apperley and P. R. Slater, *Dalton Trans.*, 2012, **41**, 261.
22 D. Ivanova, E. M. C. L. G. P. Lima, A. Kovalevsky, F. M. L. Figueiredo, V. V. Kharton and F. M. B. Marques, *Ionics*, 2008, **14**, 349.
23 X. Guo and R. Waser, *Prog. Mater. Sci.*, 2006, **51**, 151.
24 M. J. Verkerk, A. J. A. Winnubst and A. J. Burggraaf, *J. Mater. Sci.*, 1982, **17**, 3113.
25 S. P. S. Badwal and J. Drennan, *J. Mater. Sci.*, 1987, **22**, 3231.
26 M. L. Mecartney, *J. Am. Ceram. Soc.*, 1987, **70**, 54.
27 S. P. S. Badwal and J. Drennan, *J. Mater. Sci.*, 1989, **24**, 88.
28 D. Ivanova, A. Kovalevsky, V. V. Kharton and F. M. B. Marques, *Bol. Soc. Esp. Ceram. V*, 2008, **47**, 201.
29 B. C. H. Steele, *Solid State Ionics*, 2000, **129**, 95.
30 T. S. Zhang, J. Ma, S. H. Chan, P. Hing and J. A. Kilner, *Solid State Sci.*, 2004, **6**, 565.
31 S. P. S. Badwal, *Solid State Ionics*, 1995, **76**, 67.
32 J. M. Porras-Vazquez and P. R. Slater, *Fuel Cells*, 2012, **12**, 1056.
33 C. A. Hancock and P. R. Slater, *Dalton Trans.*, 2011, **40**, 5599.
34 A. C. Larson and R. B. V. Dreele, General Structure Analysis System (GSAS) program. Rep. No. LA-UR-86748, Los Alamos National Laboratory, Los Alamos, CA, 1994.
35 S. McIntosh, J. F. Vente, W. G. Haije, D. H. A. Blank and H. J. M. Bouwmeester, *Solid State Ionics*, 2006, **177**, 1737.
36 V. A. Cherepanov, T. V. Aksenova, L. Ya. Gavrilova and K. N. Mikhaleva, *Solid State Ionics*, 2011, **188**, 53.
37 V. Cherepanov, T. Aksenova, E. Kiselev and L. Gavrilova, *Solid State Sci.*, 2008, **10**, 438.

38 S. Kobayashi, Y. Tokuda, T. Mizoguchi, N. Shibata, Y. Sato, Y. Ikuhara and T. Yamamoto, *J. Appl. Phys.*, 2010, **108**, 124903.

39 D. Johnson, *ZView: a Software Program for IES Analysis, Version 2.8*, Scribner Associates, Inc., Southern Pines, NC, 2008.

40 B. L. Phillips, R. J. Kirkpatrick and J. G. Thompson, *Phys. Rev. B: Condens. Matter*, 1991, **43**, 13280.

41 A. Rolle, S. Boulfrad, K. Nagasawa, H. Nakatsugawa, O. Mentre, J. Irvine and S. Daviero-Minaud, *J. Power Sources*, 2011, **196**, 7328.